REPORTS

VOLCANOLOGY

The Yellowstone magmatic system from the mantle plume to the upper crust

Hsin-Hua Huang,[1,2]* Fan-Chi Lin,[1] Brandon Schmandt,[3] Jamie Farrell,[1] Robert B. Smith,[1] Victor C. Tsai[2]

The Yellowstone supervolcano is one of the largest active continental silicic volcanic fields in the world. An understanding of its properties is key to enhancing our knowledge of volcanic mechanisms and corresponding risk. Using a joint local and teleseismic earthquake *P*-wave seismic inversion, we revealed a basaltic lower-crustal magma body that provides a magmatic link between the Yellowstone mantle plume and the previously imaged upper-crustal magma reservoir. This lower-crustal magma body has a volume of 46,000 cubic kilometers, ~4.5 times that of the upper-crustal magma reservoir, and contains a melt fraction of ~2%. These estimates are critical to understanding the evolution of bimodal basaltic-rhyolitic volcanism, explaining the magnitude of CO_2 discharge, and constraining dynamic models of the magmatic system for volcanic hazard assessment.

The interaction of the North American Plate moving southwestward across a mantle plume created the Snake River Plain, a bimodal basalt-rhyolite volcanic system dating to 16.5 million years ago (Ma) (*1*). The Yellowstone volcanic field that sits at the eastern end of the plain is the youngest manifestation of the hotspot and is characterized by extensive earthquakes (*2*, *3*), episodic ground deformation (*4*), high heat flux averaging 2000 mW m^{-2} (*2*, *5*), and the largest continental hydrothermal system in the world (*6*, *7*). The most recent cataclysmic eruption occurred at 0.64 Ma and created the 40 km × 60 km Yellowstone caldera, which is filled with rhyolitic lava flows as young as 70,000 years (Fig. 1). Earlier teleseismic studies have imaged a west-northwest–dipping plume extending into the top of the lower mantle (*8*–*11*). Local earthquake tomography and waveform modeling studies have revealed an upper-crustal magma reservoir between 5 and 16 km depth (*3*, *12*, *13*), of which the shallowest portion correlates with the largest area of hydrothermal activity and extends 15 km northeast of the caldera (*3*). Even with a large volume of >4000 km^3 and a high melt fraction of up to 32% (*2*, *3*, *13*), this upper-crustal reservoir cannot account for the large CO_2 flux of 4.5×10^7 kg daily and requires additional input of basaltic magma invading the lower to middle crust (*6*, *7*). Moreover, it is unclear how the mantle plume interacts with the crustal volcanic system. The connection between the shallow magma reservoir (above 16 km depth) and the deep mantle plume (below 60 km depth) is therefore a critical component to understand the entire Yellowstone magmatic system but has never been imaged distinctly, despite other geophysical and geologic

[1]Department of Geology and Geophysics, University of Utah, Salt Lake City, UT 84112, USA. [2]Seismological Laboratory, California Institute of Technology, Pasadena, CA 91125, USA. [3]Department of Earth and Planetary Sciences, University of New Mexico, Albuquerque, NM 87131, USA.
*Corresponding author. E-mail: hsinhua.huang@utah.edu

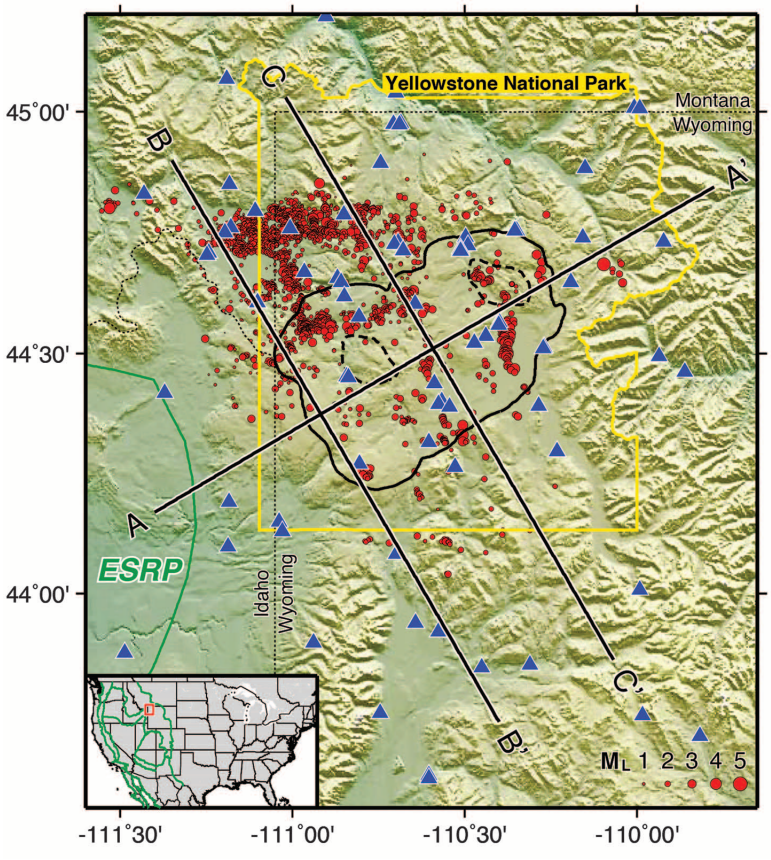

Fig. 1. Map of the seismic stations used in this study and the *P*-wave velocity cross-section locations in the Yellowstone area. Stations and earthquakes are denoted by blue triangles and red dots, respectively. Black solid and dashed lines outline the Late Quaternary Yellowstone caldera and resurgent domes. Green lines represent the tectonic division of the Eastern Snake River Plain (ESRP). Yellow and thin dotted lines are the border of Yellowstone National Park and the surrounding state borders, respectively. Locations of the cross sections in Fig. 3 are shown by thick black lines with labels. The inset map shows the location of the Yellowstone area (red box) and the major tectonic boundaries (green lines) in the western United States.

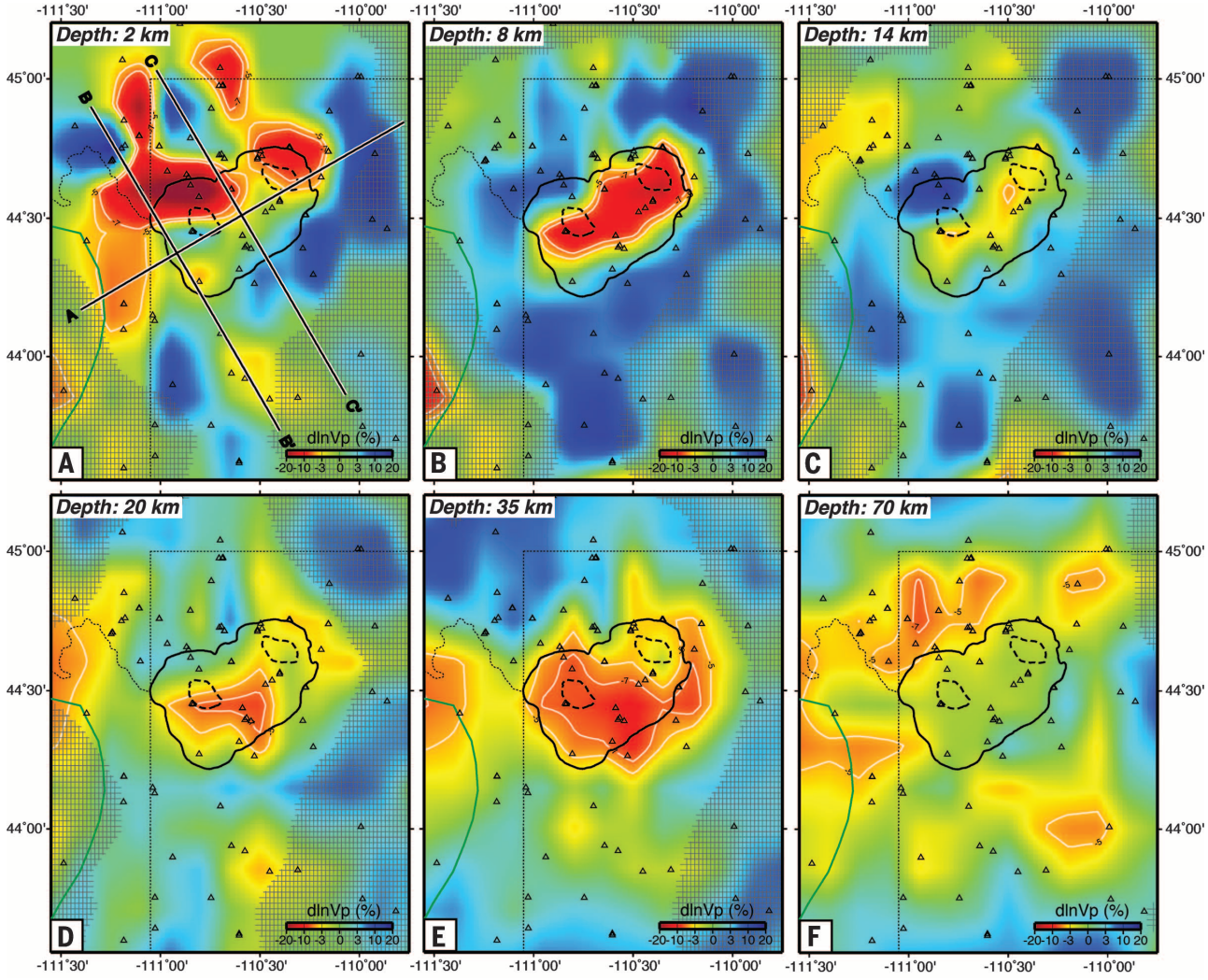

Fig. 2. Depth slices of the Yellowstone tomographic *P*-wave model. (**A** to **E**) Crustal velocity structures; (**F**) upper-mantle velocity structure. Black solid and dashed lines outline the 0.64 Ma caldera and resurgent domes. The green line is the northeast end of the Eastern Snake River Plain. White lines denote the 5% and 7% *P*-wave velocity reduction contours. Poorly resolved areas are shaded according to the index of resolvability, *R*, converted from the checkerboard test results (*25*).

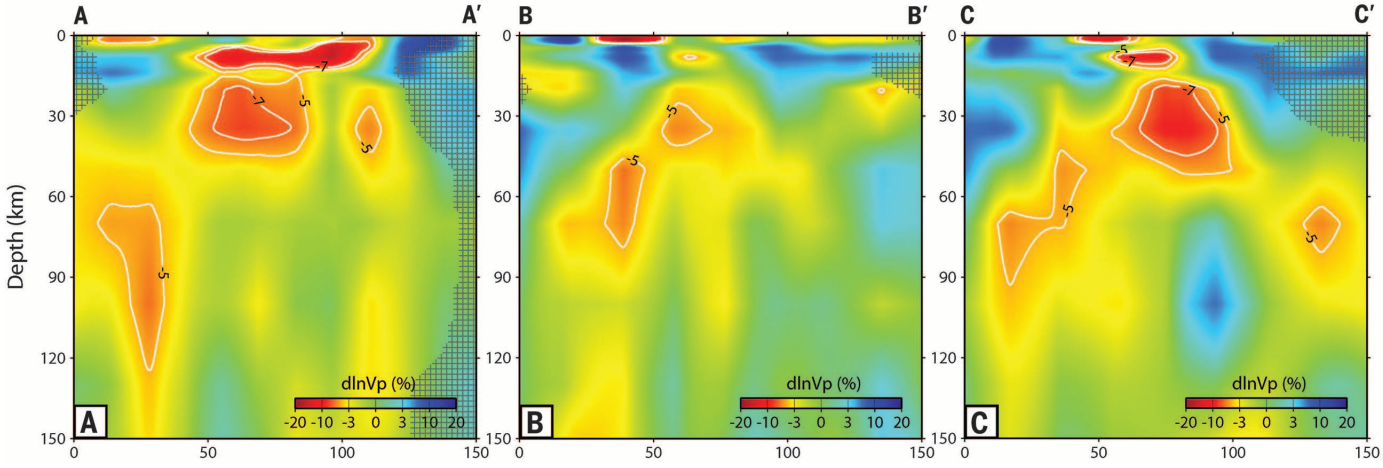

Fig. 3. Cross sections of the Yellowstone tomographic *P*-wave model. (**A** to **C**) The crustal magmatic reservoirs and the mantle plume are demonstrated in northeast-southwest (A) and northwest-southeast [(B) and (C)] directions, respectively. Map-view locations of the cross sections are shown in Fig. 1. White lines denote the 5% and 7% *P*-wave velocity reduction contours. Poorly resolved areas are shaded according to the index of resolvability, *R*, converted from the checkerboard test results (*25*).

evidence that hypothesizes the presence of a continuous crustal magma body (*2*, *5*, *7*).

Imaging the position and size of the entire volcanic plumbing system is also important to constrain magmatic dynamics modeling for further hazard assessment (*14*). Many local seismic array experiments have been conducted on volcanoes such as Askja, Iceland (*15*); Axial, Juan de Fuca mid-ocean ridge (*16*); Kilauea, Hawaii (*17*); and Mount St. Helens, Washington (*18*). A common observation of these experiments is an imaged shallow low-velocity body (LVB) at depths of 5 to 10 km, which is often interpreted as a magma reservoir. Several of these studies also image the top of a second LVB at greater crustal depths (*18*, *19*); however, they usually quickly lose resolution with depth because of the limited array aperture and the shallowly distributed earthquakes (often less than ~10 km depth). Large arrays for teleseismic tomography can only focus on mantle images and poorly resolved crustal structures. A complete framework of the mantle-crust volcanic system under volcanoes has not yet been elucidated.

By combining data from the dense seismic arrays of the Yellowstone, Teton, and Snake River Plain (SRP) regional seismic networks, the NOISY array (*20*), and the wide-aperture EarthScope Transportable Array (Fig. 1), we present an image of the entire volcanic plumbing system beneath the Yellowstone caldera and reveal a large basaltic magma reservoir in the lower to middle crust by using a joint tomographic inversion of local and teleseismic earthquake data (*21*–*23*). The seismic data used in this study were compiled from previous studies (*3*, *24*) and consist of 47,815 *P*-wave first arrivals from 4520 local earthquakes and 4605 relative arrival times from 329 teleseismic earthquakes. A local earthquake inversion is first conducted to obtain a three-dimensional initial crustal model and reduce the dominance of the local data prior to the joint inversion (*25*).

We found a large east-northeast–west-southwest elongated LVB beneath the Yellowstone caldera (Fig. 2, A to C, and Fig. 3A) at depths shallower than 20 km, consistent with previous studies (*3*, *25*). However, at depths of 20 to 50 km, another larger LVB with >5% *P*-wave velocity (V_P) reduction also emerges in our model (Fig. 2, D and E, and Fig. 3, A and C). From cross section AA′ (Fig. 1 and Fig. 3A), it is clear that this deeper LVB is immediately beneath the shallow LVB. The existence of the lower-crustal LVB and the separation between the two imaged crustal LVBs are validated through characteristic-model synthetic tests and finite-frequency analysis (*25*), indicating that the deep crustal LVB is a separate magma reservoir in the middle to lower crust, based on a Moho depth of ~45 km in this area (*26*). The LVB separates into two zones northwest and southeast of the caldera at mantle depths of ~70 km (Fig. 2F). The orientation of the northwestern portion agrees with the extension of the SRP in a northeast-southwest direction, implying the track of the North American Plate across the Yellowstone plume (*2*, *10*). In cross sections BB′ and CC′, this low-velocity zone that dips ~60° northwestward is consistent with the plume geometry determined in previous studies (*8*–*10*). In contrast, the southeastern low-velocity zone is relatively smaller and localized, terminating at a depth of 100 km (Fig. 3C).

The V_P reduction of >5% within the imaged crustal LVBs is difficult to explain by temperature and composition alone and implies the presence of melts (*25*). We assume a 5% V_P reduction as being diagnostic of partial melt (*3*) to quantitatively estimate the volume of crustal melt. Weaker anomalies may also be partly explained by partial melt, but tradeoffs with temperature or composition variations and tomographic resolution prevent these weaker anomalies from being robustly interpreted as melt. Using this conservative proposition results in volume estimates of ~46,000 km^3 for the lower-crustal LVB and ~10,000 km^3 for the upper-crustal LVB. These estimates agree well with the sizes and depths of the basaltic and rhyolitic magma reservoirs interpreted by geochemical studies (*6*, *7*, *27*). The melt fraction of the upper-crustal LVB has been previously estimated to range from 5 to 32% (*2*, *3*, *13*). With an average V_P of 5.21 km/s calculated over the volume of the upper-crustal LVB, we estimate a melt fraction of ~9% (*25*), based on a velocity-melt fraction relation derived for the Yellowstone granite-rhyolite-melt system (*13*). For the lower-crustal LVB, we assume similar elastic properties between the lower crust and the uppermost mantle and use previously proposed partial derivatives of V_P with respect to melt fraction for a peridotite-basalt-melt system (table S2). Given the calculated average V_P reduction of 6.56%, a ~2% fraction of basaltic partial melts is preferred (*25*). Multiplying the melt fraction of each LVB by its volume gives ~900 km^3 of rhyolitic melts and also ~900 km^3 of basaltic partial melts. These estimates provide an overall volume estimate that is comparable to the explosive material volumes of the last three Yellowstone giant eruptions at 2.1 Ma (2500 km^3), 1.3 Ma (280 km^3), and 0.64 Ma (1000 km^3) (*1*). Although lower-crustal basaltic melts are not expected to contribute to the caldera-forming eruptions, and the upper-crustal melts are unlikely to erupt at one time, both melt volumes can feed smaller eruptions. Assuming a CO_2 degassing rate of 4.5×10^7 kg per day, 50% of which comes from subsurface magma discharge (*28*), the addition of a basaltic lower-crustal reservoir can provide a sufficient influx (*25*) for the reported ~15,000-year history of the intensive hydrothermal degassing system (*29*).

Our seismic images depict characteristics of the entire Yellowstone magmatic system from the upper mantle to the crust (Fig. 4) in which the west-northwest–dipping plume is the magmatic source that generates the mafic/basaltic partial melts that intrude into the lower crust, fractionate, and melt the crust to produce more silicic magma, and then intermittently ascend to shallower depths to form the dominantly rhyolitic reservoir at depths of 4 to 14 km beneath the Yellowstone caldera. Because volcanic sills act as traps that accumulate upward-migrating magmatic fluids to form a magma reservoir (*2*, *3*, *6*, *30*–*32*), the two large LVBs observed in our model suggest the presence of two sill complexes in the upper and lower crust that are likely linked by dikes. This layered structure of basaltic intrusions was also suggested for the volcanic crustal structure in the nearby eastern Snake River Plain (*33*). This model may thus be representative of other bimodal basaltic-rhyolitic volcanoes around the

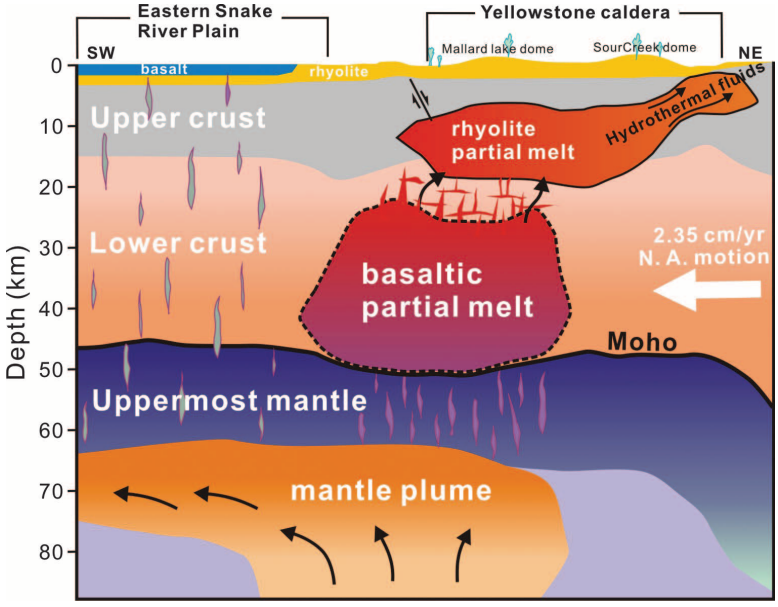

Fig. 4. Schematic model for the Yellowstone crust–upper mantle magmatic system. The orientation of the model is along the cross section AA′ in Fig. 3. The geometry of the upper- and lower-crustal magma reservoirs is based on the contour of 5% V_P reduction in the tomographic model. The dashed outline of the lower-crustal magma reservoir indicates the larger uncertainties in its boundaries relative to that of the upper reservoir (*25*). The white arrow indicates the North American plate motion of 2.35 cm/year.

world. The estimates of volume and geometry of crustal magma reservoirs may also be critical for realistic modeling magmatic system dynamics (*14*) that in turn could provide further information for volcanic hazard models.

REFERENCES AND NOTES

1. R. L. Christiansen, *U.S. Geol. Surv. Prof. Pap. 729-G*, 145 (2001).
2. R. B. Smith *et al.*, *J. Volcanol. Geotherm. Res.* **188**, 26–56 (2009).
3. J. Farrell, R. B. Smith, S. Husen, T. Diehl, *Geophys. Res. Lett.* **41**, 3068–3073 (2014).
4. W. L. Chang, R. B. Smith, C. Wicks, J. M. Farrell, C. M. Puskas, *Science* **318**, 952–956 (2007).
5. K. R. DeNosaquo, R. B. Smith, A. R. Lowry, *J. Volcanol. Geotherm. Res.* **188**, 108–127 (2009).
6. J. B. Lowenstern, S. Hurwitz, *Elements* **4**, 35–40 (2008).
7. S. Hurwitz, J. B. Lowenstern, *Rev. Geophys.* **52**, 375–411 (2014).
8. H. Yuan, K. Dueker, *Geophys. Res. Lett.* **32**, L07304 (2005).
9. M. Xue, R. M. Allen, *J. Geophys. Res.* **115**, B07303 (2010).
10. M. Obrebski, R. M. Allen, F. Pollitz, S. H. Hung, *Geophys. J. Int.* **185**, 1003–1021 (2011).
11. B. Schmandt, K. Dueker, E. Humphreys, S. Hansen, *Earth Planet. Sci. Lett.* **331–332**, 224–236 (2012).
12. S. Husen, R. B. Smith, G. P. Waite, *J. Volcanol. Geotherm. Res.* **131**, 397–410 (2004).
13. R. Chu, D. V. Helmberger, D. Sun, J. M. Jackson, L. Zhu, *Geophys. Res. Lett.* **37**, L01306 (2010).
14. M. Paulatto *et al.*, *Geochem. Geophys. Geosyst.* **13**, Q01014 (2012).
15. M. A. Mitchell, R. S. White, S. Roecker, T. Greenfield, *Geophys. Res. Lett.* **40**, 5040–5046 (2013).
16. M. West, W. Menke, M. Tolstoy, S. Webb, R. Sohn, *Nature* **413**, 833–836 (2001).
17. E. M. Syracuse *et al.*, *J. Geophys. Res.* **115**, B10310 (2010).
18. G. P. Waite, S. C. Moran, *J. Volcanol. Geotherm. Res.* **182**, 113–122 (2009).
19. I. Koulakov *et al.*, *J. Volcanol. Geotherm. Res.* **263**, 75–91 (2013).
20. K. J. Seats, J. F. Lawrence, *Geophys. Res. Lett.* **41**, 8277–8282 (2014).
21. S. W. Roecker *et al.*, *J. Geophys. Res.* **98**, 15779 (1993).
22. D. Zhao, A. Hasegawa, H. Kanamori, *J. Geophys. Res.* **99**, 22313–22329 (1994).
23. H.-H. Huang *et al.*, *Geophys. Res. Lett.* **41**, 10.1002/2014GL061115 (2014).
24. B. Schmandt, F. C. Lin, *Geophys. Res. Lett.* **41**, 6342–6349 (2014).
25. See supplementary materials on *Science* Online.
26. W. Shen, M. H. Ritzwoller, V. Schulte-Pelkum, *J. Geophys. Res.* **118**, 262–276 (2013).
27. S. M. White, J. A. Crisp, F. J. Spera, *Geochem. Geophys. Geosyst.* **7**, Q03010 (2006).
28. C. Werner, S. Brantley, *Geochem. Geophys. Geosyst.* **4**, 1061 (2003).
29. R. O. Fournier, *Annu. Rev. Earth Planet. Sci.* **17**, 13–53 (1989).
30. K. Jaxybulatov *et al.*, *Science* **346**, 617–619 (2014).
31. C. Annen, J. D. Blundy, R. S. J. Sparks, *J. Petrol.* **47**, 505–539 (2006).
32. A. Gudmundsson, *Tectonophysics* **500**, 50–64 (2011).
33. J. W. Shervais, S. K. Vetter, B. B. Hanan, *Geology* **34**, 365 (2006).

ACKNOWLEDGMENTS

Data were collected from the Yellowstone seismograph network operated by the University of Utah, the NSF-funded EarthScope project, and a temporary seismic array operated by Stanford University. All waveform data used in this project can be obtained through the IRIS Data Management Center. Supported by the University of Utah, the University of Utah Seismograph Stations, NSF grants CyberSEES-1442665, EAR-1252191, and EAR-03233309 (in support of the EarthScope Transportable Array), and the Brinson Foundation and Carrico funds.

SUPPLEMENTARY MATERIALS

www.sciencemag.org/content/348/6236/773/suppl/DC1
Materials and Methods
Figs. S1 to S7
Tables S1 to S3
References (*34–48*)

20 January 2015; accepted 1 April 2015
Published online 23 April 2015;
10.1126/science.aaa5648

QUANTUM OPTICS

Quantum dynamics of an electromagnetic mode that cannot contain *N* photons

L. Bretheau, P. Campagne-Ibarcq, E. Flurin, F. Mallet, B. Huard*

Electromagnetic modes are instrumental in building quantum machines. In this experiment, we introduce a method to manipulate these modes by effectively controlling their phase space. Preventing access to a single energy level, corresponding to a number of photons *N*, confined the dynamics of the field to levels 0 to *N* – 1. Under a resonant drive, the level occupation was found to oscillate in time, similarly to an *N*-level system. Performing a direct Wigner tomography of the field revealed its nonclassical features, including a Schrödinger cat–like state at half period in the evolution. This fine control of the field in its phase space may enable applications in quantum information and metrology.

The manipulation of a quantum system usually involves the control of its Hamiltonian in time. An alternative route consists in effectively tailoring its Hilbert space dynamically. This can be done by restricting the system evolution to a subset of possible states. When even a single energy level is disabled, the system evolution is deeply modified and is ruled by the so-called quantum Zeno dynamics (QZD) (*1–5*). As the name suggests, the level blockade can be realized by repeatedly checking whether the level is occupied, owing to the inherent back action of quantum measurements (*1*, *2*, *6*). Alternatively, as in the present experiment, QZD can be achieved by blocking the level using a strong, active coupling to an ancillary quantum system (*3–5*), without any measurement (*7*). These ideas have recently been demonstrated for atoms, using either Rb Bose-Einstein condensates (*8*) or Rydberg atoms (*9*). However, the dynamics of these systems are intrinsically confined to a finite number of energy levels. Here, using a circuit quantum electrodynamics architecture, we implement QZD of light. With its large number of energy levels and ease of control, a single electromagnetic mode offers a wider and more controllable phase space than atoms and two-level systems.

The principle of our experiment is shown in Fig. 1. One cavity mode of frequency f_c is coupled to a qubit of frequency f_q. For a large enough detuning, their evolution can be described by the dispersive Hamiltonian $hf_c a^\dagger a + hf_q|e\rangle\langle e| - h\chi a^\dagger a|e\rangle\langle e|$, where h is Planck's constant, $a^\dagger$ is the ladder operator, and $|e\rangle$ is the excited state of the qubit. The last term describes the frequency shift of the cavity (qubit) $-\chi$, which occurs when the qubit (cavity) is excited by one extra quantum of energy. Owing to this shift, a tone at frequency $f_q - N\chi$ addresses only the transition between states $|N\rangle \otimes |g\rangle$ and $|N\rangle \otimes |e\rangle$ for level widths smaller than χ (*10*); here, $|g\rangle$ is the ground state of the qubit. These levels then hybridize and repel each other. Their splitting is given by the Rabi frequency Ω_R, at which the qubit population would oscillate in the case where the cavity is in state $|N\rangle$ (Fig. 1). Any transition to level N is now forbidden when the cavity is driven at resonance. Schematically, level N has been moved out of the harmonic ladder (Fig. 1). Then, starting from the ground state, the electromagnetic mode is confined to levels 0 to $N-1$, whereas the qubit remains in its ground state. The field dynamics is dramatically changed, resembling that of an N-level system, and nonclassical states similar to "Schrödinger cat states" develop.

In the experiment, we use the fundamental mode of a three-dimensional (3D) microwave cavity made out of bulk aluminum, which resonates at $f_c = 7.804$ GHz. This mode is off-resonantly coupled to a superconducting qubit (*11*) with bare frequency $f_q = 5.622$ GHz and dispersive frequency shift $\chi = 4.63$ MHz. The cavity exit rate $\gamma_c = (1.3\ \mu s)^{-1}$ is dominated by the coupling rate to two transmission lines connected to the cavity, which are used for both driving and the readout of the system. The relaxation rate $\gamma_1 = (11.5\ \mu s)^{-1}$ and decoherence rate $\gamma_2 = (8.9\ \mu s)^{-1}$ of the ancillary qubit are an order of magnitude smaller.

The experiment is performed by first turning on the blocking tone at $f_q - N\chi$. For the level blockade to be effective, we choose $\Omega_R = 6.24$ MHz, much larger than the level frequency width, which is about γ_c. Then, the cavity is driven at frequency $f_d \approx f_c$ for a time t varying up to a few μs. The drive power is fixed throughout the experiment and would lead to an amplitude displacement rate ε_d of about $3\ \mu s^{-1}$ in the cavity, were there neither damping nor nonlinearities. At time t, both the blocking signal and the cavity drive are turned off, and the field state is measured. Two measurement schemes are used to characterize the cavity state. Both methods use as a probe the same qubit that is used to provide the level blockade.

The first method consists in measuring the probability P_k for the field to host k photons. To do so, a selective π pulse is applied to the qubit at frequency $f_q - k\chi$ so that it gets excited if k photons are in the cavity. Measuring

Laboratoire Pierre Aigrain, Ecole Normale Supérieure–PSL Research University, CNRS, Université Pierre et Marie Curie–Sorbonne Universités, Université Paris Diderot–Sorbonne Paris Cité, 24 Rue Lhomond, 75231 Paris Cedex 05, France.
***Corresponding author. E-mail: benjamin.huard@ens.fr**

The Yellowstone magmatic system from the mantle plume to the upper crust

Hsin-Hua Huang, Fan-Chi Lin, Brandon Schmandt, Jamie Farrell, Robert B. Smith and Victor C. Tsai

Science **348** (6236), 773-776.
DOI: 10.1126/science.aaa5648originally published online April 23, 2015

Yellowstone's missing magmatic link

Yellowstone is an extensively studied "supervolcano" that has a large supply of heat coming from a pool of magma near the surface and the mantle below. A link between these two features has long been suspected. Huang *et al.* imaged the lower crust using seismic tomography (see the Perspective by Shapiro and Koulakov). Their findings provide an estimate of the total amount of molten rock beneath Yellowstone and help to explain the large amount of volcanic gases escaping from the region.

Science, this issue p. 773; see also p. 758